TU Delft

Delft University of Technology

Wideband Modeling of CMOS Schottky Barrier Diode Detectors for THz Radiometry

van Berkel, Sven; Malotaux, Satoshi; De Martino, Carmine; Spirito, Marco; Cavallo, Daniele; Neto, Andrea; Llombart, Nuria

DOI
10.1109/TTHZ.2021.3085137

Publication date
2021

Document Version
Accepted author manuscript

Published in
IEEE Transactions on Terahertz Science and Technology

Citation (APA)
van Berkel, S., Malotaux, S., De Martino, C., Spirito, M., Cavallo, D., Neto, A., & Llombart, N. (2021). Wideband Modeling of CMOS Schottky Barrier Diode Detectors for THz Radiometry. *IEEE Transactions on Terahertz Science and Technology*, *11*(5), 495-507. Article 9444666. https://doi.org/10.1109/TTHZ.2021.3085137

Important note
To cite this publication, please use the final published version (if applicable).
Please check the document version above.

Copyright
Other than for strictly personal use, it is not permitted to download, forward or distribute the text or part of it, without the consent of the author(s) and/or copyright holder(s), unless the work is under an open content license such as Creative Commons.

Takedown policy
Please contact us and provide details if you believe this document breaches copyrights.
We will remove access to the work immediately and investigate your claim.

This work is downloaded from Delft University of Technology.
For technical reasons the number of authors shown on this cover page is limited to a maximum of 10.

Wideband Modeling of CMOS Schottky Barrier Diode Detectors for THz Radiometry

Sven van Berkel§, *Member, IEEE*, Satoshi Malotaux§, *Student Member, IEEE*, Carmine de Martino, *Student Member, IEEE*, Marco Spirito, *Member, IEEE*, Daniele Cavallo, *Senior Member, IEEE*, Andrea Neto, *Fellow, IEEE*, and Nuria Llombart, *Fellow, IEEE*

***Abstract*—A complete system modeling and characterization of a wideband differential THz direct detector, integrated in a commercial CMOS technology, is presented. The detector consists of a recently developed double leaky slot lens antenna that operates from 200 GHz to 600 GHz in combination with a differential Schottky Barrier Diode (SBD) direct detection circuit. The proposed methodology, starting from low frequency measurements on a standalone SBD, is able to adequately model the spectral radiometric performance. The system Noise Equivalent Power (NEP) is characterized from 325 GHz to 500 GHz in excellent agreement with the proposed system model. The measured NEP, $20\,\mathrm{pW}/\sqrt{\mathrm{Hz}}$ minimum and $90\,\mathrm{pW}/\sqrt{\mathrm{Hz}}$ frequency averaged, is compromised w.r.t. the average NEP of $2.7\,\mathrm{pW}/\sqrt{\mathrm{Hz}}$ that was initially predicted by simulations using the process design kit (PDK) model, since the available SBDs are operating beyond their cut-off frequency. The diodes and models provided by the PDK proved to be inaccurate in predicting circuit behavior at these high frequencies. By using the proposed analysis and modeling approaches, an accurate wideband antenna-detector co-design could be applied for future passive THz imaging applications based on CMOS technologies.**

***Index Terms*—submillimeter-wave, terahertz, ultrawideband, passive imaging, radiometry, schottky barrier diode, NEP, NETD**

I. Introduction

THz imaging and sensing is appealing for several types of applications [1]–[4], ranging from astronomy [5], security screening [6], [7], biology and medicine [8] to automotive radar [9]. However, the current integration capabilities of required active components still restrains a widespread deployment of commercial applications [4], [10], [11]. For instance, the realization of fully passive THz direct detectors in CMOS technologies would enable low-cost imaging applications. In order to achieve the required performance for passive imaging, a wideband antenna should efficiently couple incident radiation over a few hundreds of GHz of bandwidth to detectors that are characterized with a Noise Equivalent Power (NEP) in the order of a $\mathrm{pW}/\sqrt{\mathrm{Hz}}$ [12]. Efficient wideband antenna operation is demonstrated with an on-chip ring antenna in SiGe-HBT technology [13] and with a double leaky slot antenna in CMOS technology [14] in combination with a silicon lens. Low NEP detectors have been demonstrated in high performance III-V technologies [15]. In the lower performance CMOS technologies, however, achieving sub-$\mathrm{pW}/\sqrt{\mathrm{Hz}}$ NEPs is proven to be difficult [16]. Previous CMOS related publications have reported detectors based on pn-junction diodes with a NEP of 56 $\mathrm{pW}/\sqrt{\mathrm{Hz}}$ at 781 GHz [17], Schottky Barrier Diodes (SBDs) with a NEP of 29 $\mathrm{pW}/\sqrt{\mathrm{Hz}}$ at 280 GHz [18], [19], differential Diode-connected NMOS transistors have been demonstrated with a NEP of 12.6 $\mathrm{pW}/\sqrt{\mathrm{Hz}}$ at 823 GHz [20] and differentially connected MOSFETs with a NEP of 14 $\mathrm{pW}/\sqrt{\mathrm{Hz}}$ at 724 GHz [21]. The high cut-off frequency of SBDs makes them very attractive in submm-wave applications [22] and are in fact the preferred detector in GaAs technologies [23]. A NEP of 12 $\mathrm{pW}/\sqrt{\mathrm{Hz}}$ at 855 GHz is achieved in the same technology as the one considered here by using nFETs in a differential configuration [24]. The state-of-the-art NEP of 3.5 $\mathrm{pW}/\sqrt{\mathrm{Hz}}$ at 300 GHz is just recently presented using a differential transistor pair at zero bias [25]. The performance in terms of bandwidth in [14] and NEP in [25] is approaching the level where first THz passive imagers might be realized [12].

An accurate modeling of the antenna-detector combination and read-out circuit over a large frequency band is vital to enable passive THz imaging in silicon technology [13]. For resistive self-mixing FETs, a close antenna-detector co-design, taking into account antenna efficiency and antenna-detector impedance matching, is realized in [26]–[28] by extending the Dyakonov and Shur plasma-wave theory [29] for an accurate system responsivity and NEP prediction. Alternatively, FETs can also be optimized using non-physical Taylor expansions or Volterra series [25], [30], [31]. The NEP of the SBDs, presented in [18], [19], and diode connected NMOS transistors in [20], were modeled using an equivalent lumped element circuit of a SBD with a high-frequency device analysis approach that was introduced in [32]. In the referred literature, however, the

§: Both authors contributed equally to this work.

Manuscript received August XX, 2020; revised XX XX, XXXX; accepted X XX, XXXX. Date of publication XX XX, XXXX; date of current version August 17, 2020. This research is supported by the Dutch Technology Foundation STW (Project Terahertz silicon-Integrated CAMera, TiCAM, 13325). The work of - S. van Berkel was partly funded - N. Llombart was funded - by the European Research Council starting Grant LAA-THz-CC 639749. (Corresponding author: Sven van Berkel.) The authors would like to thank Global Foundries for the technology access. Also, the authors would like to thank Maarten Vertregt from NXP Semiconductors for the technical support during the project and the fruitful technology related discussions.

S. van Berkel, D. Cavallo, A. Neto and N. Llombart are with the THz Sensing Group, Delft University of Technology, Delft 2828 CD, The Netherlands (e-mail: S.L.vanBerkel@ieee.org; D.Cavallo@tudelft.nl; A.Neto@tudelft.nl; N.LlombartJuan@tudelft.nl).

S. Malotaux, C. de Martino and M. Spirito are with the Electronic Circuits and Architectures (ELCA) group, Delft University of Technology, Delft 2828 CD, The Netherlands (e-mail: E.S.Malotaux@tudelft.nl; C.DeMartino-1@tudelft.nl; M.Spirito@tudelft.nl).

Color versions of one or more of the figures in this paper are available online at http://ieeexplore.ieee.org.

Digital Object Identifier XX.XXXX/TTHZ.2020.XXXXXXX

© 2021 IEEE. Personal use of this material is permitted. Permission from IEEE must be obtained for all other uses, in any current or future media, including reprinting/republishing this material for advertising or promotional purposes, creating new collective works, for resale or redistribution to servers or lists, or reuse of any copyrighted component of this work in other works

system is analyzed in combination with a narrowband antenna. For future wideband applications the direct detection system should be optimized over the very large frequency bandwidth simultaneously to optimize temperature sensitivity [12].

This work extends the high-frequency modeling approach of a SBD, as introduced in [32] and applied in [18], [19], to predict the radiometric performance of a wideband double leaky slot lens antenna coupled to a differential SBD detection circuit that is connected to a load resistor for a voltage read-out. The design of the antenna is recently presented in [14] to operate with a 57% average efficiency from 200 GHz to 600 GHz, while complying with strict minimum metal density rules. The THz direct detector is shown in Fig. 1, showing a photograph of the silicon elliptical lens and a micrograph of the fabricated CMOS chip containing the double leaky slot. Here, a system modeling approach is presented that predicts the radiometric performance in terms of temperature sensitivity and NEP by using an equivalent circuit that can be constructed from low-frequency measurements on a standalone SBD.

The remainder of this contribution is structured as follows. In Sec. II, the figures of merit in the design of passive THz imaging cameras are introduced. In Sec. III, the lumped element circuit model of a SBD is introduced and is constructed from measurements on a standalone SBD. The performance in terms of diode efficiency and current responsivity is evaluated. In Sec. IV, the SBD model is extended to a complete system model of the THz direct detector, including the antenna and the interface with the detection circuit. In Sec. V, the performance of the direct detector is presented in terms of antenna patterns, RMS output noise voltage and system voltage responsivity.

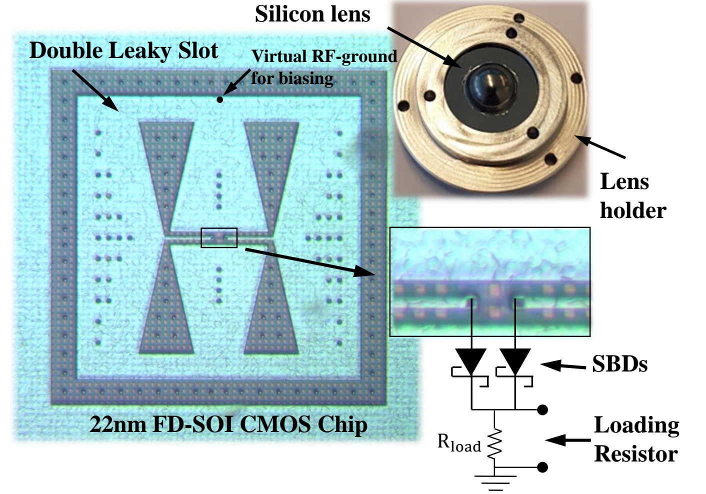

Fig. 1: THz direct detector. The detector consists of a double leaky slot lens antenna [14] that is connected to a differential SBD direct detection circuit.

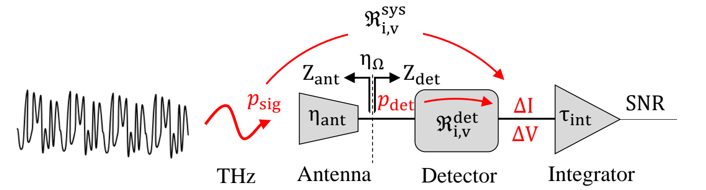

Fig. 2: Schematic of an incoherent (direct) detection architecture, indicating its three main components; the antenna, detector and integrator.

II. Passive THz Imaging

A schematic of a direct detection architecture is shown in Fig. 2. In such architecture, an antenna with a frequency dependent antenna efficiency $\eta_{\text{ant}}(f)$, couples an incident THz signal, defined with a spectral power $p_{\text{sig}}(f)$ in units of W/Hz, to a detector circuit that contains devices with a non-linear behavior, such as transistors and diodes. In radiometry, considering incoherent and distributed sources in the Rayleigh-Jeans limit as studied in [12], the spectral incident power for a single polarized antenna $p_{\text{sig}}(f) \approx k_B T_S$ is constant over frequency with k_B being Boltzmann's constant and T_S the source temperature.[1] A portion of the power that is available at the antenna will be reflected due to the impedance mismatch between the antenna input impedance, $Z_{\text{ant}}(f)$, and detection circuit input impedance, $Z_{\text{det}}(f)$, which should be conjugally matched to maximize the matching efficiency, $\eta_\Omega(f)$. The detector is biased to allow a certain DC current flowing through the detector and voltage drop over the detector in the considered case where the detector is biased via a load resistor. Due to the non-linear current-voltage relationship of the detector, the power that is absorbed in the detection circuit, $p_{\text{det}}(f)$, then induces an average incremental increase in DC-voltage drop over the load resistor, ΔV. This RF-to-DC voltage conversion is quantified via the detector voltage responsivity, $\Re_v^{\text{det}}(f)$ in units of V/W, as (1):

$$\Delta V = \int_{\Delta f_{\text{RF}}} p_{\text{det}}(f) \Re_v^{\text{det}}(f) df \tag{1}$$

, where Δf_{RF} is the absolute frequency bandwidth of the direct detector. For uncooled detectors, the SNR is usually limited by the noise that is introduced by the detection circuit. The measured signal, after detection, can be integrated for τ_{int} seconds in order to achieve a sufficient Signal-to-Noise Ratio (SNR), provided that the system is stable without Flicker-noise contributions. The root-mean-square (RMS) noise voltage V_n, after integration, can be written as (2):

$$V_n = \frac{v_n}{\sqrt{2\tau_{\text{int}}}} \tag{2}$$

, where v_n is the spectral RMS noise voltage, within the post-detection bandwidth, in $V/\sqrt{\text{Hz}}$.[2] The SNR can then be expressed as:

$$\text{SNR} = \frac{\Delta V}{V_n} = \frac{\sqrt{2\tau_{\text{int}}}}{v_n} \int_{\Delta f_{\text{RF}}} p_{\text{det}}(f) \Re_v^{\text{det}}(f) df \tag{3}$$

For narrowband direct detection systems, both spectral power and voltage responsivity can be approximated by their value at center frequency f_c. The total power absorbed in the detection circuit is then $P_{\text{det}} \approx p_{\text{det}}(f_c)\Delta f_{\text{RF}}$. In this

[1] In the case of isolated (or active) sources, $p_{\text{sig}}(f)$ will also depend on the shape of the antenna beam and frequency.

[2] A 1 Hz post-detection bandwidth is equivalent to 0.5 second of integration time [33], [34].

approximation, the SNR for narrowband systems, SNR_{NB}, can be written in a form that is commonly found in literature [33], [34]:

$$\text{SNR}_{\text{NB}} = P_{\text{det}} \frac{\Re_v^{\text{det}}}{v_n} \sqrt{2\tau_{\text{int}}} = \frac{P_{\text{det}}}{\text{NEP}_{\text{det}}} \sqrt{2\tau_{\text{int}}} \tag{4}$$

, where the detector NEP (NEP_{det}) is defined as $\text{NEP}_{\text{det}} = v_n/\Re_v^{\text{det}}$ and represents the amount of power absorbed by the detection circuit that results in a SNR = 1 after 0.5 second of integration time. For wideband direct detectors, the incident power and detector NEP can fluctuate significantly over frequency and therefore the spectral integration in (3) should be retained. The SNR for wideband direct detectors, SNR_{WB}, can then equivalently be written as:

$$\text{SNR}_{\text{WB}} = \sqrt{2\tau_{\text{int}}} \int_{\Delta f_{\text{RF}}} \frac{p_{\text{det}}(f)}{\text{NEP}_{\text{det}}(f)} df \tag{5}$$

In radiometry, differences in the apparent temperature of the incoherent source that is seen by the beam pattern of the imager, results in differences in received signal power. The temperature difference of incoherent sources, that gives rise to a SNR of unity is a useful figure of merit and is defined as the temperature sensitivity, i.e. the Noise Equivalent Temperature Difference (NETD) of the radiometer. In [12], the NETD is derived by starting from the narrowband approximated SNR (4) in the case of distributed sources that are in the Rayleigh-Jeans limit of Planck's law. Instead, by starting from the wideband SNR expression (5) and by recalling $p_{\text{det}}(f) = p_{\text{sig}}(f)\eta_{\text{ant}}(f)\eta_\Omega(f)$ with $p_{\text{sig}}(f) = k_B T_S$, the NETD is derived to be:

$$\text{NETD} = \frac{1}{k_B \sqrt{2\tau_{\text{int}}} \int_{\Delta f_{\text{RF}}} \frac{\eta_{\text{ant}}(f)\eta_\Omega(f)}{\text{NEP}_{\text{det}}(f)} df} \tag{6}$$

The NEP and voltage responsivity of the full THz direct detector system, NEP_{sys} and $\Re_v^{\text{sys}}$, including the impedance matching of the antenna detector combination as well as the optical efficiency of the lens antenna, can now be defined as:

$$\text{NEP}_{\text{sys}}(f) = \frac{\text{NEP}_{\text{det}}(f)}{\eta_{\text{ant}}(f)\eta_\Omega(f)} = \frac{v_n}{\Re_v^{\text{sys}}(f)} \tag{7a}$$

$$\Re_v^{\text{sys}}(f) = \Re_v^{\text{det}}(f)\eta_{\text{ant}}(f)\eta_\Omega(f) \tag{7b}$$

The system (or optical) NEP and responsivity, NEP_{sys} (7a) and $\Re_v^{\text{sys}}$ (7b), are generally reported in literature.

A qualitative study of NETD in a security screening scenario is presented in [35], where it is shown that a sub-Kelvin temperature sensitivity is required for effective concealed weapon detection. Such requirement will most likely be similar for other low-cost THz imaging applications. In order to reach such high performance, (6) shows the necessity of using an accurate system modeling approach, in terms of system NEP and its different spectral components, that allows for an antenna-detector co-design.

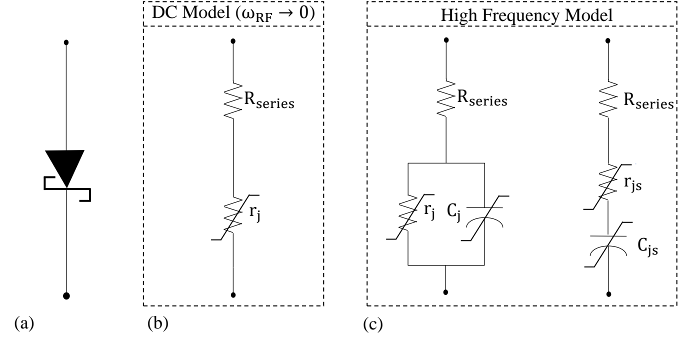

Fig. 3: DC- and High-frequency models of a SBD. (a) Symbol of SBD. (b) The DC-model is shown, consisting of the junction resistance and series resistance of the SBD. (c) The high-frequency model is shown with on the left-hand side the physical model indicating the junction capacitance and on the right-hand side a series equivalent model to analyze the power transfer efficiency.

III. SBD Equivalent Circuit

The considered THz direct detector, shown in Fig. 1, is based on a differential SBD detection circuit. Its performance will be modeled starting from a derivation of the current responsivity of a single SBD, $\Re_i^{\text{diode}}$, as shown in Fig. 3(a). The diode current responsivity is defined as an average incremental change in current, ΔI, flowing through the diode as a result of P_{diode} Watt of power absorbed in the SBD, $\Re_i^{\text{diode}} = \Delta I / P_{\text{diode}}$, and can be derived using the lumped element circuit model of a SBD. At DC, the diode can be accurately represented using the schematic shown in Fig. 3(b), where R_{series} is the series resistance, accounting for losses of the interconnecting materials before and after the diode junction and r_j is the junction resistance of the diode, representing the junction as function of biasing voltage. Using the IV-curve, the current responsivity at low frequency, $\Re_i^{\text{diode}}(\omega_{RF} \to 0)$, can be analyzed as is well described in [32] and applied in [18], [19]. Suppose a signal of $V_{\text{D}} = V_0 + A\cos(\omega_{RF} t)$ is impinging on the diode with IV-relationship $I_{\text{D}} = f(V_{\text{D}})$, where V_0 is the biasing voltage over the diode with an RF-signal superimposed. By expanding the IV-curve in a 4th order Taylor power series around the biasing voltage V_0, the average incremental change in current, ΔI, can be evaluated. The expansion can then subsequently be used to evaluate the average absorbed signal power in the SBD, P_{diode}. After dividing the resulting terms, the current responsivity for $\omega_{RF} \to 0$ can be approximated to be:

$$\Re_i^{\text{diode}}(\omega_{RF} \to 0) \approx \frac{1}{2} \frac{f^{(2)}}{f^{(1)}} \tag{8}$$

where $f^{(i)}$ is the i-th order derivative of $I_D = f(V_D)$ with respect to V_D and evaluated in V_0. However, this responsivity assumes that the voltage drop of the RF-signal occurs over the total diode resistance $R_{\text{diode}} = R_{\text{series}} + r_j$. In reality, at higher frequencies, $\omega_{RF} > 0$, the junction capacitance of the diode should be accounted for as shown in the left-hand side of Fig. 3(c). The junction capacitance and series resistance are the main parasitic elements of the SBD that decrease performance. The rectifying characteristic of a diode is the result of the non-linear behavior of the junction current as

function of the voltage over the junction. Only RF-power that is actually absorbed in the junction, P_j, contributes to the incremental DC-current ΔI. Therefore, for higher capacitance and series resistance, the current responsivity will decrease. The junction admittance is rewritten to its equivalent series impedance, as in [18], where r_{js}, in the right-hand side of Fig. 3(c), is the series equivalent of the junction resistance and can be defined as:

$$r_{js} = \mathrm{Re}\left[\frac{r_j \frac{1}{j\omega_{\mathrm{RF}} C_j}}{r_j + \frac{1}{j\omega_{\mathrm{RF}} C_j}}\right] = \frac{r_j}{1 + (\omega_{\mathrm{RF}} C_j r_j)^2} \tag{9}$$

The junction capacitance is effectively short-circuiting the junction at higher frequencies. The power transfer efficiency, η_{PTE}, of the power absorbed by the complete diode, P_{diode}, to the absorbed power in the junction, P_j, can be written as [32]:

$$\eta_{\mathrm{PTE}}(\omega_{RF}) = \frac{P_j}{P_{\mathrm{diode}}} = \frac{r_{js}}{r_{js} + R_{\mathrm{series}}} \tag{10}$$

So in fact, the current responsivity derived from the IV-curve (8) is for a frequency $\omega_{RF} \to 0$ with a power transfer efficiency of: $\eta_{\mathrm{PTE}}(\omega_{RF} \to 0) = r_j/(r_j + R_{\mathrm{series}})$. An expression for the current responsivity, that is also valid at high frequencies, $\Re_i^{\mathrm{diode}}(\omega_{RF})$, can then be derived from the low-frequency current responsivity as follows:

$$\Re_i^{\mathrm{diode}}(\omega_{RF}) = \eta_{\mathrm{PTE}}(\omega_{RF}) \frac{\Re_i^{\mathrm{diode}}(\omega_{RF} \to 0)}{\eta_{\mathrm{PTE}}(\omega_{RF} \to 0)} \tag{11}$$

The diode current responsivity, valid at submm-wave frequencies, can be derived from the IV-curve and bias dependent junction capacitance.

PDK SBD and Measured SBD

This work uses the smallest SBDs available in the PDK of the technology. The minimum dimension allowed for the considered SBD is $1.6\,\mu\mathrm{m} \times 1.6\,\mu\mathrm{m}$. Smaller diodes are desirable in terms of NEP as the shot-noise contribution is reduced for a smaller magnitude in diode current. A schematic side-view and top-view of the SBD are shown in Fig. 4(a) and (b) respectively. To validate the actual performance of the fabricated SBD, the device model is constructed from low-frequency measurements on a standalone device. The standalone SBD is fabricated alongside the THz direct detector together with dedicated calibration structures, for characterization purposes. These structures featured SOLT/TRL compatible de-embedding fixtures that allows DUT characterization at their device terminals from DC to the WR-2.2 frequency band that are implemented similar to the ones presented in [36].

The IV-curve, simulated using the models provided by the PDK, including parasitic extraction of the additional interconnect (approximately $2\,\Omega$) to the device, is shown by the black-curve in Fig. 5(a). The device simulation is performed in the software tool Virtuoso Analog Design Environment by Cadence. The IV-characteristic, of the standalone SBD embedded in a fixture, is measured using a DC-probe station. By using the *Thru* fixture from one of the on-chip calibration standards, it is measured that the fixture itself, in absence

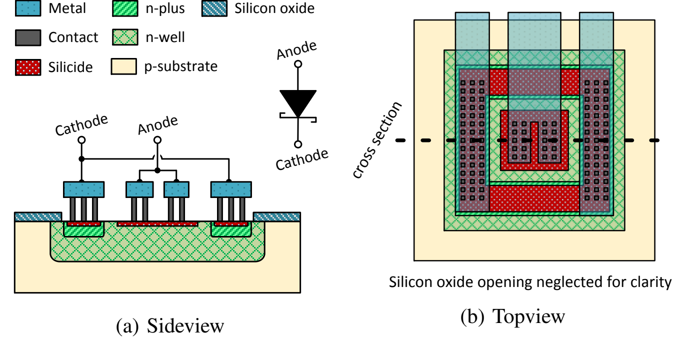

(a) Sideview (b) Topview

Fig. 4: Schematic view of the Schottky barrier diode that is used in the detection architecture.

of the SBD, has an ohmic resistance of approximately 11Ω in order to correct the raw measurement. The measured IV-curve is shown by the blue curve in Fig. 5(a). The IV-curves can be separated in two distinct regions. The section of the curve at low biasing voltages, displays a diode characteristic where the current increases exponentially. In this region, a good agreement exists between the simulated and fabricated diode. Instead, after the *knee*, the curve behaves linear as the current through the branch is now limited by the series resistance, $r_j \ll R_{\mathrm{series}}$. The lower knee of the measured IV-curve indicates a higher series resistance than predicted. This can be quantified from the inverse of the derivative of the IV-curve, which gives the total diode resistance in DC, $R_{\mathrm{diode}} = R_{\mathrm{series}} + r_j$, as shown in Fig. 5(b). The two components are highlighted in the figure. The measured series resistance of 135 Ω is significantly larger than the PDK series resistance of 10 Ω.

The junction capacitance is extracted from a measurement at $10\,\mathrm{GHz}$ using a probe station and a PNA-X N5242A from Keysight. The setup is calibrated using a Line (Thru), Reflect, Match (LRM) calibration up to the metal-1 terminals, i.e. the anode and cathode of the SBD. The junction capacitance, C_j, can be extracted from the measured S-parameters according to the high-frequency model in Fig. 3(c), and is shown in Fig. 5(c) where it is compared with simulation. The measured junction capacitance is higher than simulated using the PDK, an increase from $8\,\mathrm{fF}$ to $20\,\mathrm{fF}$ at a diode biasing voltage of $0.6\,\mathrm{V}$. As a result of this discrepancy, the diode cut-off frequency is now approximately $f_T = 1/(2\pi \cdot R_{\mathrm{series}} \cdot C_j) = 60\,\mathrm{GHz}$ versus $2\,\mathrm{THz}$ as predicted by the PDK simulation. This formula is only valid for $R_{\mathrm{series}} \gg R_j$ [32], [37].

From the simulated and measured IV-curves and junction capacitance, the equivalent SBD circuit from Fig. 3 can be constructed and the diode performance can be analyzed. The diode efficiency (10), predicted by the equivalent SBD circuits constructed from the SBD simulated using the model provided by the PDK (*PDK SBD*) and the *Measured SBD*, are shown in Fig. 5(d) and Fig. 5(e) respectively. It can be seen that the junction of the diode is barely capable of rectifying the RF-signal and the diode has less than a few percent of efficiency for frequencies higher than 400 GHz. The impact can also be seen in the diode current responsivity (11) as shown in Fig. 5(f) at $f_{\mathrm{RF}} = 200\,\mathrm{GHz}$, $400\,\mathrm{GHz}$ and $600\,\mathrm{GHz}$.

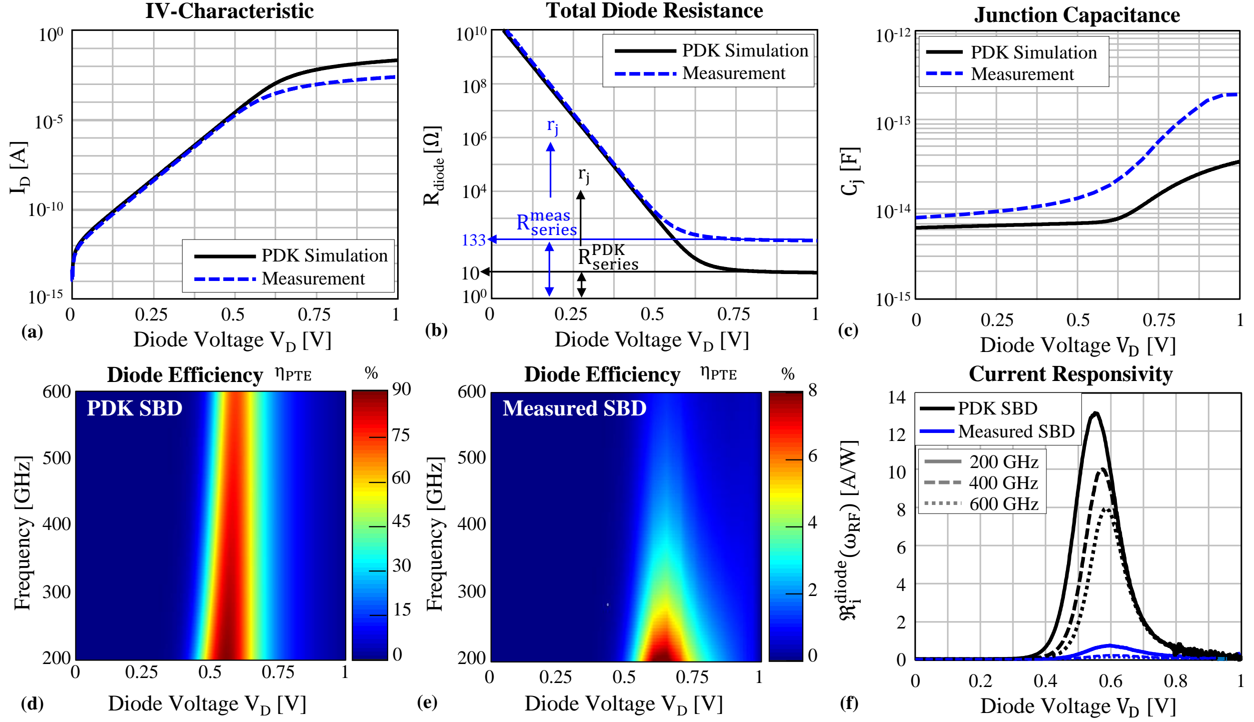

Fig. 5: SBD characterization using the simulations in PDK of the technology (black) and low-frequency measurements (blue). (a) IV-curve, I_D. (b) Total diode resistance R_{diode}. (c) Junction capacitance, C_j. (d) Modeled power transfer efficiency, $\eta_{\text{PTE}}(\omega_{\text{RF}})$, using the SBD simulated in the PDK. (e) Modeled power transfer efficiency, $\eta_{\text{PTE}}(\omega_{\text{RF}})$, using the SBD that is characterized with low-frequency measurements. (f) High frequency diode current responsivity, $\Re_i^{\text{diode}}$.

The compromised cut-off frequency prohibits the realization of passive imaging. However, SBDs integrated in CMOS technologies have been characterized in literature with a series resistance of $10\,\Omega$ to $20\,\Omega$ and a junction capacitance of 5 fF to 9 fF in [18], [19], [22]. To demonstrate the potential of using those SBDs, combined with the wideband leaky-wave antenna in [14], for future passive imaging application, the next section will derive the THz direct detector equivalent circuit for predicting the system NEP. The derivation is performed using the IV-curve and capacitance as provided by the PDK (referred to as *PDK SBD*) as well as by using the measured IV-curve and capacitance (referred to as *Measured SBD*).

IV. Differential SBD Direct Detector

A simplified circuit schematic of the THz direct detector, introduced in Fig. 1, is shown in Fig. 6(a). The antenna is a double leaky slot lens antenna, recently presented in [14], operating over a large frequency band from 200 GHz to 600 GHz. The SBD devices are set in a differential topology with the anode of the devices connected to the terminals of the antenna and cathodes connected together. The symmetry of the antenna-SBD combination results in an AC-ground between the cathodes. This AC-ground, confines the RF-current path to the antenna terminals and SBDs while the DC-/low frequency read-out network can safely be connected at this point. Both devices are biased through an RF cold-point in the antenna ground plane, as indicated in Fig. 1. Differential read-out schemes are commonly used in THz direct detection circuits [24], [38], [39]. An additional pair of diodes is placed next to

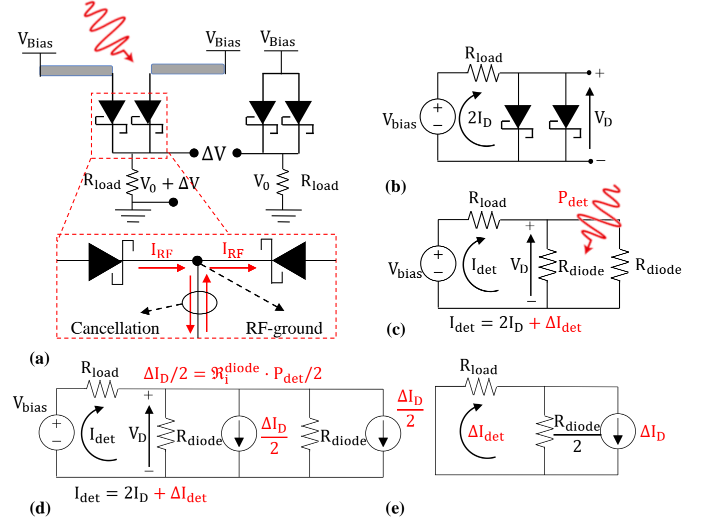

Fig. 6: Detector architecture used for the THz direct detection system (a) and DC-equivalent circuit model of a single branch (b). In (c), the SBDs are replaced with their small-signal resistances. An incremental change in DC-current flowing through the load resistance, ΔI_{det}, is the result of absorbed power P_{det}, represented by the incremental current sources in (d). Using the superposition principle, the equivalent circuit can be simplified to (e) to derive the incremental detector current.

the detecting pair that is connected to the antenna terminals. The additional pair forms a reference branch in order to provide a pseudo-differential output and improve the circuit immunity to supply noise and electromagnetic interference

from the outside environment. Each SBD pair is connected to a load resistor with resistance R_{load}, to convert the rectified current, ΔI, into a voltage output, ΔV.

A. Detector Circuit

The equivalent circuit schematic, of only the detector branch, is shown in Fig. 6(b). The current flowing through the detector, I_D, is determined by the voltage drop across the diodes, V_D. Using either the simulated or measured $I_D = f(V_D)$ relationship of the diode, the required pixel biasing voltage, V_{bias}, in order to reach a desired diode biasing point can be calculated as function of the value of the load resistance as: $V_{\text{bias}} = 2I_D(V_D)R_{\text{load}} + V_D$. The value of the load resistor is $R_{\text{load}} = 2\,\text{k}\Omega$ and is chosen such that the optimal biasing conditions can be achieved with a pixel biasing voltage of $V_{\text{bias}} < 2\,\text{V}$ while maximizing voltage responsivity. At each diode biasing point, V_D, the small-signal model can be applied and the diode can be represented by its dynamic diode resistance $R_{\text{diode}}(V_D)$ as is shown in Fig. 6(c). Suppose that P_{det} is absorbed in the differential detector, with each SBD thus absorbing half of the power $P_{\text{det}}/2$. As quantified by the diode current responsivity (11), an average incremental DC-current of $\Delta I_D/2$ flowing through each SBD is expected. The total current flowing through the load resistance, I_{det}, now becomes: $I_{\text{det}} = 2I_D + \Delta I_{\text{det}}$. The incremental increase in current is represented by the current sources as shown in Fig. 6(d). Using the superposition principle and by considering only the incremental current contributions due to the absorbed THz power, the circuit can be simplified to Fig. 6(e) and the change in current flowing through the load resistor, ΔI_{det} can be calculated as:

$$\Delta I_{\text{det}} = \Delta I_D \frac{R_{\text{diode}}/2}{R_{\text{diode}}/2 + R_{\text{load}}} \tag{12}$$

Defining then the current responsivity of the differential detector circuit as $\Re_i^{\text{det}} = \Delta I_{\text{det}}/P_{\text{det}}$ gives:

$$\Re_i^{\text{det}} = \frac{\Delta I_{\text{det}}}{P_{\text{det}}} = \Re_i^{\text{diode}} \frac{R_{\text{diode}}/2}{R_{\text{diode}}/2 + R_{\text{load}}} \tag{13}$$

From (13), it can be seen that a high load resistor can significantly reduce the current responsivity (R_{diode} is only tens of Ohms at the optimal biasing conditions). However, the voltage responsivity, $\Re_v^{\text{det}}$, that relates the output signal ΔV, to the THz power absorbed in the entire detection circuit, P_{det}, increases linearly with the resistance and can be expressed as:

$$\Re_v^{\text{det}} = \frac{\Delta V}{P_{\text{det}}} = \Re_i^{\text{det}} R_{\text{load}} = \Re_i^{\text{diode}} \frac{R_{\text{diode}} R_{\text{load}}}{R_{\text{diode}} + 2R_{\text{load}}} \tag{14}$$

The current- and voltage responsivity for $f_{\text{RF}} = 200\,\text{GHz}, 400\,\text{GHz}$ and $600\,\text{GHz}$ for the PDK SBD are shown in Fig. 7(a) by the black lines. A harmonic balance simulation, of the complete detection circuit, is performed in Virtuoso ADE as verification of the equivalent circuit model and is shown by the dashed red lines in Fig. 7(a).

The dominant noise contributions in the considered detection architecture are Flicker-noise, shot-noise generated by the junction and Johnson (thermal) noise generated by the load

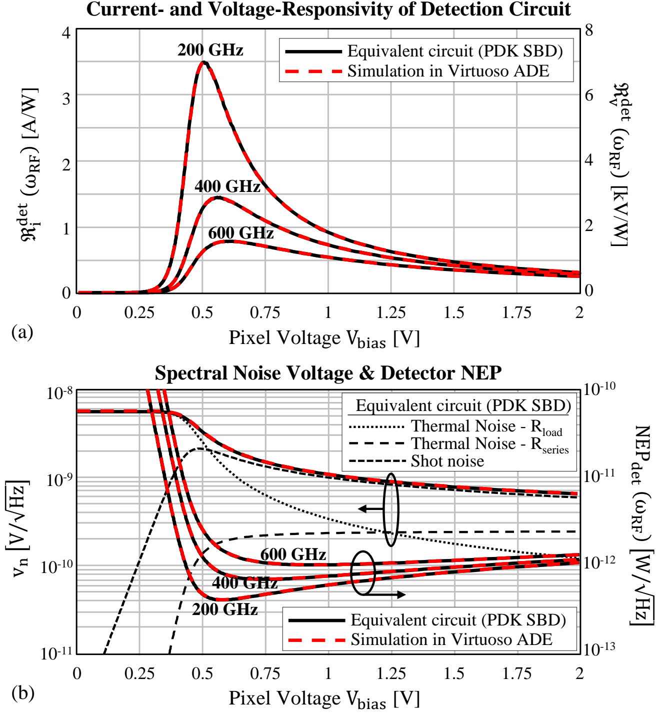

Fig. 7: Validation, in terms of responsivity and noise, of the equivalent circuit model for the PDK SBD, by means of simulations of the full direct detection circuit. A load resistor of $R_{\text{load}} = 2\,\text{k}\Omega$ is taken and the frequencies $f_{RF} = 200\,\text{GHz}, 400\,\text{GHz}$ and $600\,\text{GHz}$ are evaluated. (a) Current (13) and voltage responsivity (14). (b) On the left axis is the spectral noise voltage (15) and the individual contributions (16). On the right axis is the Detector NEP (17).

resistor and series resistance of the diode. Flicker-noise is not included in the PDK model. of the considered SBD. We will investigate the remaining (white) noise contributions, beyond the 1/f corner. In [19], a similar sized SBD is characterized with a Flicker-noise corner of approximately 4 MHz. The remaining white noise mechanisms are incoherent and the individual contributions should be summed in power. The total voltage noise, v_n in $V/\sqrt{\text{Hz}}$, can be expressed as:

$$v_n = \sqrt{|v_n^{\text{shot}}|^2 + |v_n^{R_{\text{load}}}|^2 + |v_n^{R_{\text{series}}}|^2} \tag{15}$$

where the individual contributions can be derived using circuit analysis of the detection circuit. The two parallel SBDs are analyzed with a single SBD that is defined with half the diode resistance of $R_{\text{diode}}/2$ and twice the current, $2I_D$. Shot-noise is defined with a current generator ($\sqrt{2q|2I_D|}$) in parallel of the junction ($r_j/2$) whereas thermal noise is evaluated by using a voltage generator ($\sqrt{4k_B T_n R}$) in series with either the load resistance (R_{load}) or series resistance ($R_{\text{series}}/2$). The spectral noise voltage contributions at the read-out terminals are then:

$$v_n^{\text{shot}} = \sqrt{2q|2I_D|}\frac{r_j/2}{R_{\text{diode}}/2 + R_{\text{load}}} R_{\text{load}} \tag{16a}$$

$$v_n^{R_{\text{load}}} = \sqrt{4k_{\text{B}} T_n R_{\text{load}}}\frac{R_{\text{diode}}/2}{R_{\text{diode}}/2 + R_{\text{load}}} \tag{16b}$$

$$v_n^{R_{\text{series}}} = \sqrt{4k_{\text{B}} T_n R_{\text{series}}/2}\frac{R_{\text{load}}}{R_{\text{diode}}/2 + R_{\text{load}}} \tag{16c}$$

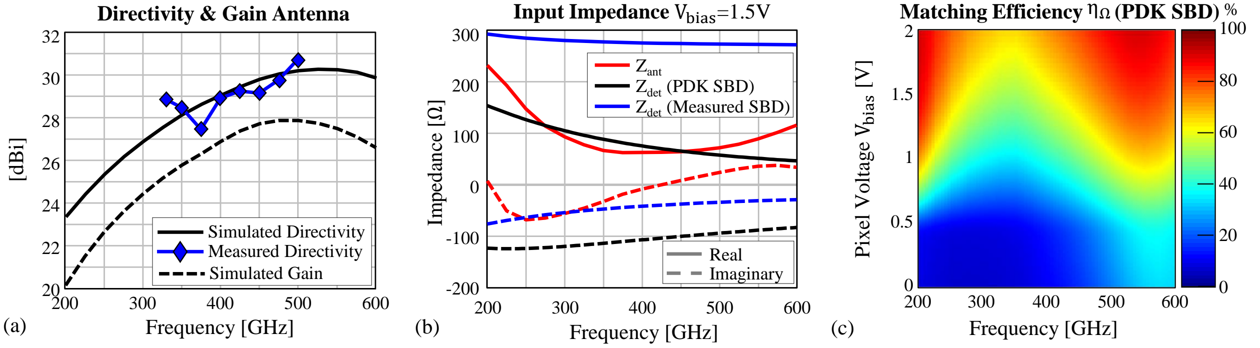

Fig. 8: Simulated antenna performance and impedance matching with detection circuit. (a) Simulated antenna directivity and gain [14] (black curves) and measured directivity from Sec. V-A (blue curve). (b) Input impedance of antenna (red) and detection circuit at 1.5 V of pixel biasing voltage. The detector input impedance simulated with the PDK SBDs (black) and measured SBDs (blue) is shown. (c) Impedance matching efficiency, as function of frequency and pixel biasing, between the antenna and detector circuit, simulated with the PDK SBDs.

In (16), q is the elementary charge, k_{B} is the Boltzmann constant and T_n is the noise temperature in Kelvin. The total noise and their components, predicted for the PDK SBD, are shown in the left y-axis of Fig. 7(b) where they are compared with the simulations of the full detection circuit in Virtuoso ADE. For low biasing voltages, the circuit is limited to the thermal noise introduced by the load resistor, whereas at higher, and optimal, biasing voltages, the noise is limited to the shot-noise of the diodes. Smaller diodes are desired to reduce this shot-noise. For the pseudo-differential read-out, using the reference branch as shown in Fig. 6(a), the spectral noise voltage is increased by a factor of $\sqrt{2}$, as the noise contributions from both branches are incoherently summed. The benefit of this configuration is however the increased immunity of the pixel to both supply noise and electromagnetic interference from outside the circuit.

From the detector voltage responsivity (14), spectral voltage noise in output (15), the detector NEP can be defined as:

$$\mathrm{NEP_{det}} = \frac{\sqrt{|v_n^{\mathrm{shot}}|^2 + |v_n^{R_{\mathrm{load}}}|^2 + |v_n^{R_{\mathrm{series}}}|^2}}{\Re_i^{\mathrm{diode}}} \frac{R_{\mathrm{diode}} + 2R_{\mathrm{load}}}{R_{\mathrm{diode}}R_{\mathrm{load}}} \tag{17}$$

The detector NEP is shown in the right y-axis of Fig. 7(b) and is verified with the harmonic balance simulation. A perfect agreement between the proposed system model and simulation exists. It is worthwhile to mention that a sub-pW/$\sqrt{\mathrm{Hz}}$ NEP is expected for the detection circuit based on the PDK SBD.

B. Antenna and Antenna-Detector Interface

The double leaky slot lens antenna, shown in Fig. 1 and recently presented in [14], has a simulated antenna directivity and gain as shown by the black curves in Fig. 8(a). The loss is relatively constant over the full frequency band with an average of 2.44 dB (57% antenna efficiency) from 200 GHz to 600 GHz. The silicon elliptical lens has a diameter of 7.6 mm and is provided with an anti-reflection coating to minimize the Fresnell loss at the lens interface. The antenna fully complies with the strict metal density rule of the considered advanced CMOS technology. In [14], it is shown that leaky-wave antennas are extremely suitable for integration in commercial CMOS processes as the impact of the metal density rules is minimized. The antenna input impedance is shown by the red curves in Fig. 8(b). The antenna input impedance should be conjugally matched to the impedance of the detection circuit to maximize the power accepted by the circuit. The input impedance of the differential detector circuit, seen from the antenna terminals, is $Z_{\mathrm{det}} = 2Z_{\mathrm{diode}}$, where Z_{diode} can be evaluated using the SBD equivalent circuit, Fig. 3. The reflection coefficient between the antenna-detector interface, indicated in Fig. 2, can be calculated as [40]:

$$\Gamma = \frac{Z_{\mathrm{det}} - Z_{\mathrm{ant}}^*}{Z_{\mathrm{det}} + Z_{\mathrm{ant}}} \tag{18}$$

from where the impedance matching efficiency, $\eta_\Omega = 1 - |\Gamma|^2$, is defined. The matching efficiency for the detection circuit based on the PDK SBD is shown in Fig. 8(c) as function of frequency and pixel biasing voltage. The detector circuit input impedance at a biasing voltage of $V_{\mathrm{bias}} = 1.5\,\mathrm{V}$ is shown in Fig. 8(b) with the black curves. Ideally, the antenna input impedance should be part of a co-design process with the input impedance of the direct detection circuit. In fact, direct detectors in CMOS processes such as transistors or diodes often have a capacitive impedance profile so that the antenna should preferably be designed with an inductive behavior [13], [41] or, alternatively, a transformer section can be used [25]. Also shown in Fig. 8(b), with the blue curves, is the input impedance of the detection circuit, biased at $V_{\mathrm{bias}} = 1.5\,\mathrm{V}$, based on the measured SBD. The real part is dominated by the increased series resistance of the SBD ($2 \times 135\,\Omega$) and is therefore not matched to the antenna.

C. System NEP and Temperature Sensitivity

The system NEP can now be predicted as $\mathrm{NEP_{sys}} = \mathrm{NEP_{det}}/(\eta_{\mathrm{ant}}\eta_\Omega)$ (7a). The optimal system NEP is at $V_{\mathrm{Bias}} \approx 1.5\,\mathrm{V}$ and is shown in Fig. 9(a) as function of frequency for the detection circuit based on the measured SBD (solid blue curve) and the PDK SBD (solid black curve). The predicted system NEP of the detector branch of the fabricated prototype is at a minimum at 200 GHz with NEP $=$ 20 pW/$\sqrt{\mathrm{Hz}}$

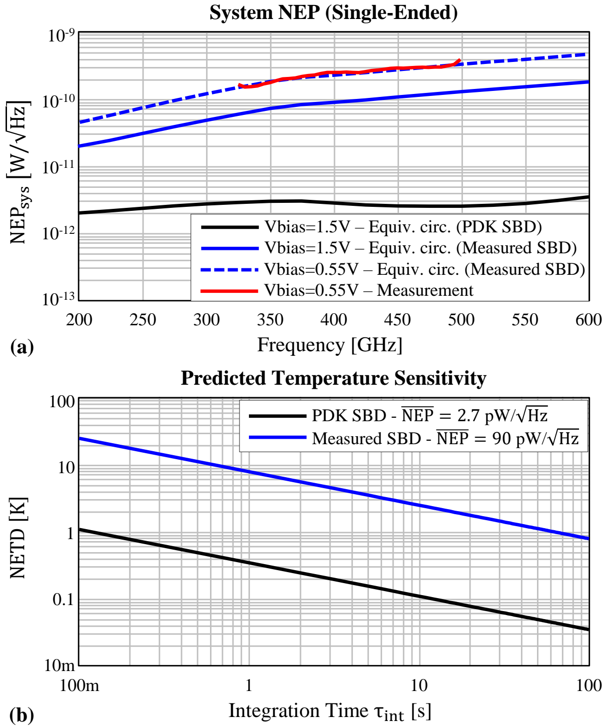

Fig. 9: Modeling of radiometric performance in terms of (a) System NEP and (b) temperature sensitivity NETD. The minimum system NEP and NETD is achieved for a biasing voltage of $V_{\text{bias}} = 1.5\,\text{V}$. Also shown in (a) are the modeled and measured NEP at $V_{\text{bias}} = 0.55\,\text{V}$ from Sec. V.

and a frequency averaged NEP of $\overline{\text{NEP}}_{\text{sys}} = 90\ \text{pW}/\sqrt{\text{Hz}}$, w.r.t. a $\overline{\text{NEP}}_{\text{sys}} = 2.7\ \text{pW}/\sqrt{\text{Hz}}$ for the PDK SBD. The flat characteristic of the system NEP for the PDK SBDs indicates the efficient utilization of a very large portion of the EM-spectrum. The temperature sensitivity (6), as function of detector integration time, is shown in Fig. 9(b). It can be seen that sub-Kelvin imaging capabilities could be achieved for NEPs of only a few $\text{pW}/\sqrt{\text{Hz}}$. The predicted NEP of the fabricated prototype is significantly higher and does not enable real-time passive imaging scenarios in the THz regime. However, the potential for realizing passive THz imaging with SBDs that are characterized with a series resistance of $10\,\Omega$ and junction capacitance of $8\,\text{fF}$, such as in [18], [19], [22], is evident.

V. Assembly and Measurement Results

The THz direct detector is characterized in the WR2.2 frequency band from $325\,\text{GHz}$ to $500\,\text{GHz}$. The assembly of the THz direct detection system, introduced in Fig. 1, is shown in Fig. 10. The diameter of the lens rim is fabricated with a $20\,\mu\text{m}$ accuracy and the lens is positioned tightly in the aluminum lens holder that is fabricated with a $50\,\mu\text{m}$ accuracy in the lens cavity. At the backside of the dielectric lens, this metallic holder contains a chip cavity that is also fabricated with a $50\,\mu\text{m}$ accuracy in width and length, where the $2\,\text{mm} \times 2.5\,\text{mm}$ CMOS-chip is positioned, so that the phase center of the radiation in the lens aligns with the focal point of the elliptical lens. Two holes, at two opposing corners of the chip cavity, allow the application of a commercial Loctite 406 superglue which, after application, flows between the chip and the dielectric lens. Some pressure is applied to minimize the thickness of the glue. The read-out terminals and power supply of the CMOS chip are bond-wired to a PCB as shown in the pictures Fig. 10(b,c). The metallic holder is attached on a fixture that can be attached to the measurement table. The direct detector will be validated in terms of lens patterns, directivity, spectral output noise and system voltage responsivity.

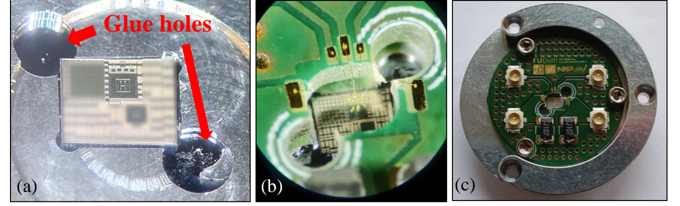

Fig. 10: Assembly of the THz direct detector. In (a), the back-side of the lens holder from Fig. 1, that contains a cavity in which the CMOS chip can be glued to the back-side of the silicon elliptical lens. (b) The CMOS chip is bondwired to a PCB that is screwed on the lens-holder (c).

A. Lens Patterns and Directivity

An overview of the measurement setup used to characterize the normalized antenna patterns and directivity is shown in Fig. 11(a) with Fig. 11(b) showing a photograph of the setup with the assembled THz direct detector, the surrounding absorbing material and the WR2.2 horn-antenna. The horn antenna is attached to a VDI WR2.2 frequency extender and placed 20 cm above the lens-antenna (in the Fraunhofer region). The horn and extender are attached on a Computer Numerical Controllable (CNC) machine and performs a $4 \times 4\ \text{cm}^2$ planar scan. Two PXI-5422 Waveform Generators from National Instruments (NI) are used to provide $100\,\text{kHz}$ synchronized square-wave signals to an IQ-mixer that modulates the signal in input of the frequency extender. The signal is modulated in order to avoid high Flicker-noise contributions and therefore increase the dynamic range of the measurement. The reduced diode efficiency of the measured SBD, as presented in Sec. III, prohibits pattern measurements with sufficient dynamic range without modulating the signal. At $100\,\text{kHz}$, the signal is still in the presence of Flicker-noise since the 1/f corner frequency is estimated to be around $4\,\text{MHz}$. The pseudo-differential output of the detector is amplified using a low-noise instrumentation voltage gain amplifier (VGA) from Analog Devices (AD8429), set to a gain of $60\,\text{dB}$ and subsequently digitized using an NI PXI-5105 ADC. A Fourier transform of the pseudo-differential read-out, ΔV, is then computed and transformed to a voltage spectrum (or power spectral density). The power located at the first harmonic (100 kHz) of the modulation frequency is the signal. The beam patterns can be calculated directly using the measured ΔV since its magnitude is proportional to the incident power ($\Delta V \propto |E|^2$). The planar scan coordinates (x, y) are translated into the uv-plane w.r.t. the lens. The

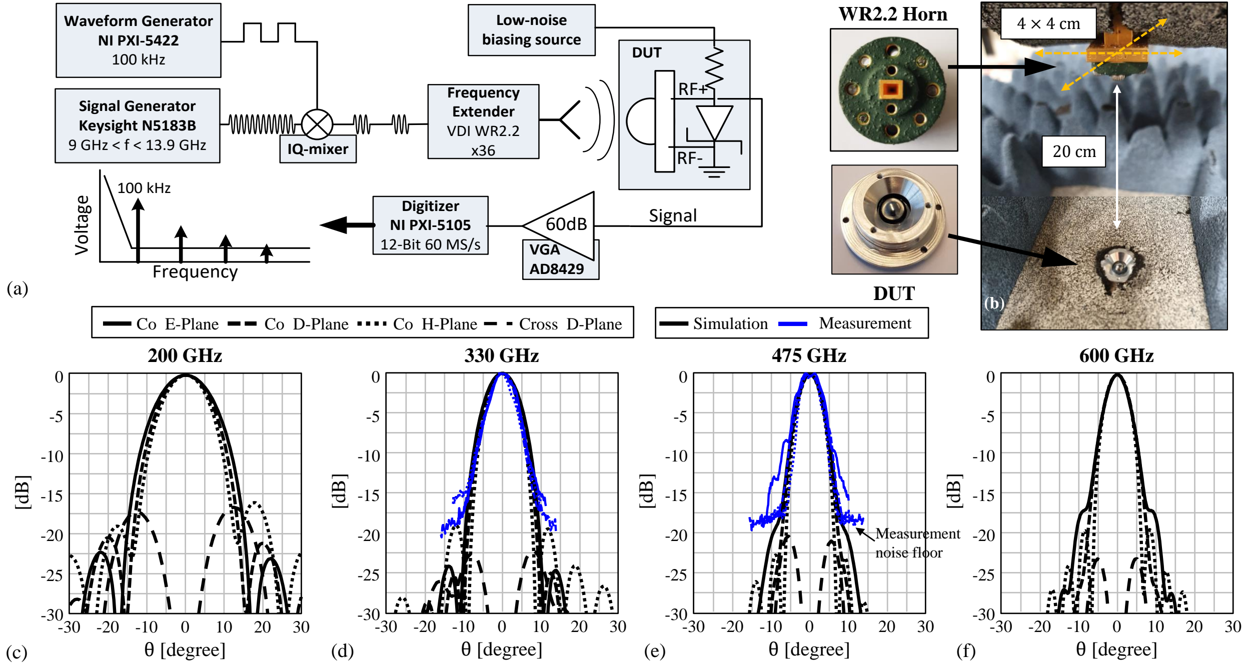

Fig. 11: Measurement setup and results of antenna beam patterns. (a) Schematic of the measurement setup of the beam patterns. (b) Photograph of the measurement setup, indicating the WR-2.2 horn antenna and the THz direct detector in the presence of absorbing material. (c-f) Simulated [14] (black curves) and measured (blue curves) beam patterns at $f_{\mathrm{RF}} = 200\,\mathrm{GHz}$, $330\,\mathrm{GHz}$, $475\,\mathrm{GHz}$ and $600\,\mathrm{GHz}$.

simulated lens patterns at $f_{\mathrm{RF}} = 200\,\mathrm{GHz}$, $330\,\mathrm{GHz}$, $475\,\mathrm{GHz}$ and $600\,\mathrm{GHz}$ are shown in Fig. 11(c-f) respectively with the black lines. The simulated lens patterns are obtained by using an in-house physical optics tool that is based on [42]. The measured beam patterns at $330\,\mathrm{GHz}$ and $475\,\mathrm{GHz}$ are shown with the blue curves, in Fig. 11(d) and (e) respectively. The dynamic range of the measurement is approximately $15\,\mathrm{dB}$ to $20\,\mathrm{dB}$. A comparison of the simulated directivity across the full band and the measured directivity in the WR-2.2 band is shown in Fig. 8(a). The low dynamic range of the pattern measurement results in some inaccuracy in the evaluation of the directivity. In [14] a similar, CPW-fed, double leaky-slot lens antenna, integrated in the same CMOS technology, is fully evaluated in terms of input impedance and gain patterns with a dynamic range of $40\,\mathrm{dB}$.

B. Noise Spectral Density

The output noise of the THz direct detector is measured after inserting the detector in a grounded metal box. The detector is biased by a battery supplied low-noise 18-bit DAC that is controlled through an SPI interface to avoid additional noise injections during the measurement that is attributed to the supply or the 50/60 Hz powergrid. The pseudo-differential output of the imager is again connected to the previously mentioned amplifier after which the output voltage is readout by a SR785 Dynamic Signal Analyzer (DSA) from Stanford Research Systems. The measured power spectral density of the noise at the output of the detector (VGA is deembedded) for different biasing voltages ranging from $V_{\mathrm{bias}} = 0\,\mathrm{V}$ to $1.5\,\mathrm{V}$ are shown in Fig. 12(a). Noise contributions of the measurement setup (measured with shorted LNA inputs) are

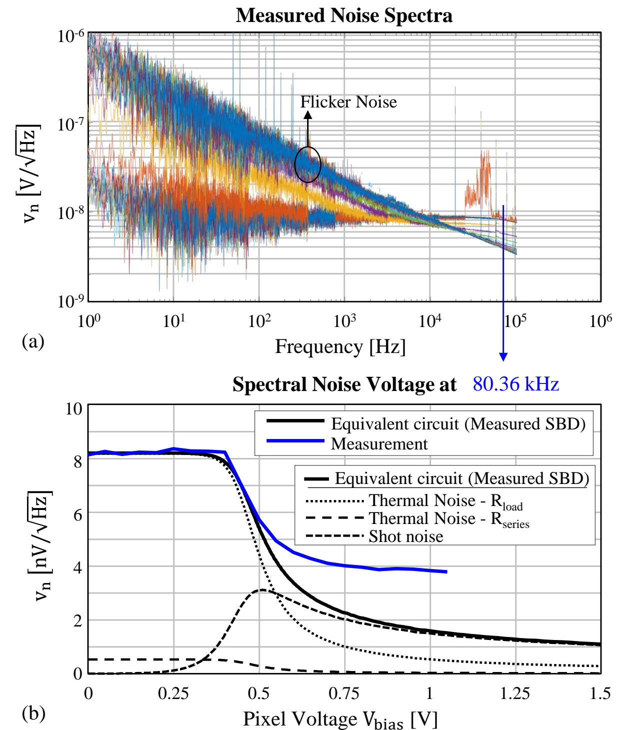

Fig. 12: Noise measurement of the THz direct detection system. For different pixel biasing voltages the noise spectrum is measured as is shown in (a). The NEP is defined using the spectral noise in the white noise region of the pixel. The spectral noise voltage, as predicted by the equivalent circuit, is shown in (b) with the black curves. The measured noise, at 80 kHz, is shown by the blue curves and is still dominated by Flicker-noise contributions for higher biasing voltages.

incoherently subtracted from the raw measurement of the DUT. The frequency range of the measured power spectral densities is limited to 100 kHz since the cut-off frequency of both the DSA and the VGA (set to 60 dBV gain) is at this frequency. The Flicker noise corner can be extrapolated to be approximately at 4 MHz for biasing voltages larger than 1V and therefore, the measurement is still performed in the frequency range where Flicker-noise can be dominant. The flicker noise of the SBD was not modeled in the provided PDK, but a comparison of the analytically calculated (15), and by simulation verified white noise level is provided in Fig. 12(b) together with the measured noise at 80 kHz. In this figure, the calculated noise contribution of both shot- and thermal noise, as described by (16), are also provided. For bias voltages from 0 to 400 mV there is good correspondence between the measured and calculated white noise level and the model presented in Sec. IV clearly matches the trend. However, at higher bias voltages the frequency limitation of the setup and the high flicker noise corner prohibited a clean measurement of the white-noise floor.

C. System Voltage Responsivity

The system voltage responsivity measurement validates the complete direct detection system in terms of antenna efficiency, antenna-detector impedance match and detector responsivity. The system voltage responsivity can be predicted as:

$$\text{Simulated } \Re_v^{\text{sys}} = \Re_v^{\text{det}} \eta_{\text{ant}} \eta_{\text{taper}} \eta_{\Omega} G_{\text{LNA}} \tag{19}$$

, where $\Re_v^{\text{det}}$ is the voltage responsivity of the detection circuit as evaluated by (14), η_{ant} is the antenna efficiency as presented in [12], $\eta_{\text{taper}} = Dir/(\pi D_{\text{lens}}/\lambda)^2$ is the tapering efficiency of the lens with diameter $D_{\text{lens}} = 7.57\,\text{mm}$ and directivity *Dir* as presented in Fig. 8(a), η_{Ω} is the antenna-detector impedance matching efficiency as predicted by the SBD equivalent circuit Fig. 3 and antenna input impedance from Fig. 8(b), and G_{LNA} is the 60 dB VGA after detection. The system voltage responsivity (19) therefore contains all performance metrics of both the antenna [12], the detection circuit and the interface between them. The simulated voltage responsivity is shown in Fig. 13(a) as function of pixel biasing voltage and frequency (WR-2.2 frequency band).

The measurement, i.e. ΔV, is performed at DC with the measurement setup as was schematically shown in Fig. 11(a), but without IQ-mixer and modulation of the signal. The power in output of the WR2.2 frequency extender, P_{horn}, is measured using a VDI Erickson PM5 power meter. Friis' transmission equation is used to evaluate the system voltage responsivity, equivalently as in [18], [19]:

$$\text{Measured } \Re_v^{\text{sys}} = \frac{\Delta V}{A_{\text{lens}} \frac{P_{\text{horn}}}{4\pi r^2} G_{\text{horn}}} \tag{20}$$

, where A_{lens} is the physical area of the lens, G_{horn} is the gain of the horn as specified by the manufacturer and $r = 10\,\text{cm}$ is the distance between the direct detector and the horn antenna. The measured system voltage responsivity (20) is shown in Fig. 13(b) as function of biasing voltage and frequency. Frequency cuts of the measured and modeled responsivity, at $f_{\text{RF}} = 330\,\text{GHz}$ and $475\,\text{GHz}$ are shown in Fig. 13(c). The reduced Tx-power in output of the frequency extender at 330 GHz increases the noise fluctuations of the measurement at this frequency point. The average voltage responsivity, over the full WR2.2. band, is also shown. By combining the measured system voltage responsivity from Fig. 13(b) and the measured spectral output noise at $V_{\text{bias}} = 0.55\,\text{V}$ from Fig. 12, at which the Flicker-noise contributions can still be neglected, we can evaluate the system NEP from (7a). This is shown in Fig. 9(a) with the red and dashed blue curves, for the single-ended detector branch. Overall, an excellent agreement

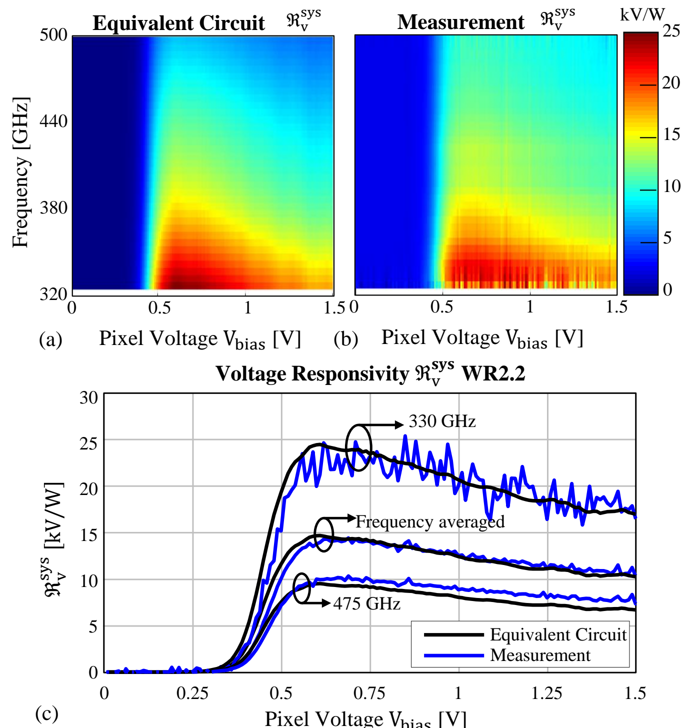

Fig. 13: System responsivity measurement and comparison with the simulation using the equivalent circuit. (a) Simulated system responsivity (19). (b) Measured system responsivity (13). (c) Comparison of simulated and measured system responsivity.

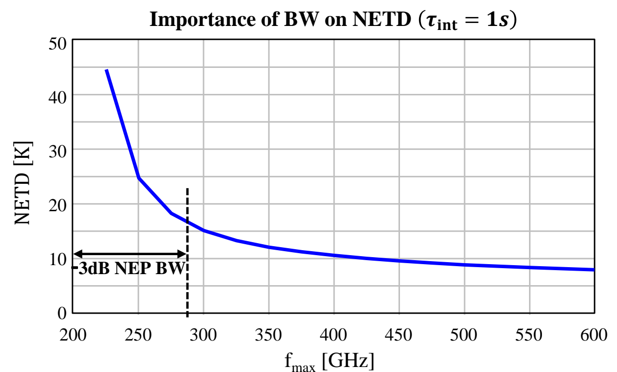

Fig. 14: Predicted NETD as function of maximum frequency for $\tau_{\text{int}} = 1s$ of integration time (21). The NETD still improves with a factor 2 by integrating power outside the -3dB BW region.

TABLE I: Modeling of Antenna-Coupled THz direct detectors in CMOS and their agreement with measurements

Reference	Detector Architecture	Modeling Methodology	Modeling and measurement BW	Wideband agreement of measurements vs model
[19]	Single SBD + patch antenna	Taylor expansion of current using lumped element circuit of SBD [32]	*Mod.*: 0.1 THz - 1 THz *Meas.*: 270 GHz - 290 GHz & 810 GHz - 870 GHz	$-^{\text{i}}$
[20]	Diode-connected NMOS + patch antenna	Current expansion in [32] is extended using an equivalent circuit model of a diode-connected NMOS	*Mod.*: 0.1 THz - 1 THz *Meas.*: 810 GHz - 850 GHz	$-+^{\text{ii}}$
[28]	Self-mixing FETs + patch antenna	Extension of the Dyakonov & Shur [29] theory where the signal is coupled to the drain	*Mod.*: 0.2 THz - 4.3 THz *Meas.*: 0.2 THz - 4.3 THz[iii]	$+^{\text{iv}}$
[31]	Differential FETs + patch antenna	Taylor expansion of the drain current	*Mod.*: 500 GHz *Meas.*: 500 GHz	$-+^{\text{v}}$
This work	Differential SBDs + load resistor + double leaky-slot antenna [14]	Taylor expansion of current [32] using a lumped element circuit that is constructed from low-frequency device measurements	*Mod.*: 200 GHz - 600 GHz *Meas.*: 325 GHz - 500 GHz	++

[i] The reported measurements in Fig. 22 and Fig. 25 of the reference show > 3 dB discrepancies in NEP modeling.
[ii] The reported measurements in Fig. 10 of the reference show a good agreement between 810 GHz and 825 GHz.
[iii] This frequency band is analyzed using ten narrowband patch antennas with different operating frequencies.
[iv] The reported measurements in Fig. 6 of the reference show a good agreement below 1 THz.
[v] Relatively good agreement is shown, but the detector is only analyzed at one discrete frequency point.

between the model and measurement exists over the full frequency band, validating the performance of the THz direct detector in terms of antenna performance and the detection circuit modeling approach, as is proposed in this contribution. In Table I, different antenna-coupled THz direct detectors from literature are reported that use a detector modeling to predict high-frequency performance. A comparison is made based on the agreement between model and measurement. Up-to-date, THz directors in CMOS have been modeled with narrowand antennas.

D. Importance of Bandwidth on NETD

Since the SBDs are operating beyond their cut-off frequency, the NEP is increasing from 20 pW/$\sqrt{\text{Hz}}$ at 200 GHz to 180 pW/$\sqrt{\text{Hz}}$ at 600 GHz, as was shown in Fig. 9(a). Consequently, the -3 dB bandwidth, i.e. a commonly reported figure of merit in the literature, has reduced to 80 GHz (from 200 GHz to 280 GHz). However, in a radiometric scenario, the NETD can still significantly improve by integrating power over a large bandwidth outside the -3dB region. This is illustrated in Fig. 14 where the NETD (6) is calculated for $\tau_{\text{int}} = 1s$ as function of the maximum frequency f_{max}:

$$\text{NETD}(f_{\text{max}}, \tau_{\text{int}} = 1s) = \frac{1}{k_B\sqrt{2}\int_{200\,\text{GHz}}^{f_{\text{max}}} \text{NEP}_{\text{sys}}^{-1}(f)df} \quad (21)$$

From Fig. 14, it can be seen that the NETD still improves with a factor of 2 from 18 K to 8 K when integrating power outside the -3dB BW region. Despite the fact that the NEP is rapidly increasing as function of f_{max}, this demonstrates the necessity of exploiting large bandwidths to realize passive THz imaging [12]. The proposed modeling approaches will enable a close antenna-detector co-design when improved diode layouts and models become available at submm-wavelength operation, provided that the signal can be modulated beyond the 1/f noise corner.

VI. Conclusion

The radiometric modeling and performance of a THz direct detection system, developed for the purpose of passive THz imaging applications is presented. The system consists of a recently developed double leaky slot lens antenna that efficiently couples radiation from 200 GHz to 600 GHz to a differential detector circuit composed of Schottky Barrier Diodes (SBDs). A derivation of the temperature sensitivity, as function of spectral Noise Equivalent Power, is presented, based on the equivalent circuit model of a SBD. The model is constructed from measurements on a standalone SBD, i.e. the IV-curve and reflection coefficient at 10 GHz and an accurate antenna modeling. These SBD low frequency measurements indicated a discrepancy in the series resistance (135 Ω vs 10 Ω) and junction capacitance (20 fF vs 8 fF) with respect to the models provided by the process design kit. Using the proposed wideband system analysis procedure, the voltage responsivity of the direct detector, that includes antenna efficiency, antenna-detector impedance matching and detector circuit performance, was predicted in excellent agreement with the measurements. This work provides an accurate modeling approach for antenna-coupled SBDs placed in a differential configuration and proving a necessary step towards the realization of future passive THz imaging applications.

References

[1] P. H. Siegel, "Terahertz technology," *IEEE Transactions on Microwave Theory and Techniques*, vol. 50, no. 3, pp. 910–928, 2002.

[2] D. L. Woolard, R. Brown, M. Pepper, and M. Kemp, "Terahertz frequency sensing and imaging: A time of reckoning future applications?" *Proceedings of the IEEE*, vol. 93, no. 10, pp. 1722–1743, 2005.

[3] W. L. Chan, J. Deibel, and D. M. Mittleman, "Imaging with terahertz radiation," *Reports on Progress in Physics*, vol. 70, no. 8, pp. 1325–1379, 2007. [Online]. Available: http://dx.doi.org/10.1088/0034-4885/70/8/R02

[4] P. Hillger, J. Grzyb, R. Jain, and U. R. Pfeiffer, "Terahertz imaging and sensing applications with silicon-based technologies," *IEEE Transactions on Terahertz Science and Technology*, vol. 9, no. 1, pp. 1–19, 2019.

[5] C. Kulesa, "Terahertz spectroscopy for astronomy: From comets to cosmology," *IEEE Transactions on Terahertz Science and Technology*, vol. 1, no. 1, pp. 232–240, 2011.

[6] J. F. Federici, B. Schulkin, F. Huang, D. Gary, R. Barat, F. Oliveira, and D. Zimdars, "THz imaging and sensing for security applications—explosives, weapons and drugs," *Semiconductor Science and Technology*, vol. 20, no. 7, pp. S266–S280, 2005. [Online]. Available: http://dx.doi.org/10.1088/0268-1242/20/7/018

[7] R. Appleby and H. B. Wallace, “Standoff detection of weapons and contraband in the 100 GHz to 1 THz region,” *Antennas and Propagation, IEEE Transactions on*, vol. 55, no. 11, pp. 2944–2956, 2007. [Online]. Available: http://ieeexplore.ieee.org/ielx5/8/4380519/04380522.pdf?tp=&arnumber=4380522&isnumber=4380519

[8] P. H. Siegel, “Terahertz technology in biology and medicine,” *IEEE Transactions on Microwave Theory and Techniques*, vol. 52, no. 10, pp. 2438–2447, 2004.

[9] M. Köhler, J. Hasch, H. L. Blöcher, and L.-P. Schmidt, “Feasibility of automotive radar at frequencies beyond 100 GHz,” *International Journal of Microwave and Wireless Technologies*, vol. 5, no. 1, pp. 49–54, 2013.

[10] K. K.O, W. Choi, Q. Zhong, N. Sharma, Y. Zhang, R. Han, Z. Ahmad, D.-Y. Kim, S. Kshattry, I. R. Medvedev, D. J. Lary, H.-J. Nam, P. Raskin, and I. Kim, “Opening Terahertz for everyday applications,” *IEEE Communications Magazine*, vol. 57, no. 8, pp. 70–76, 2019. [Online]. Available: https://dx.doi.org/10.1109/MCOM.2019.1800909

[11] E. Seok, D. Shim, C. Mao, R. Han, S. Sankaran, C. Cao, W. Knap, and O. K. K, “Progress and challenges towards Terahertz CMOS integrated circuits,” *IEEE Journal of Solid-State Circuits*, vol. 45, no. 8, pp. 1554–1564, 2010.

[12] S. van Berkel, O. Yurduseven, A. Freni, A. Neto, and N. Llombart, “THz imaging using uncooled wideband direct detection focal plane arrays,” *IEEE Transactions on Terahertz Science and Technology*, vol. 7, no. 5, pp. 481–492, 2017.

[13] J. Grzyb, M. Andree, R. Jain, B. Heinemann, and U. Pfeiffer, “A lens-coupled on-chip antenna for dual-polarization SiGe HBT THz direct detector,” *IEEE Antennas and Wireless Propagation Letters*, pp. 1–1, 2019.

[14] S. van Berkel, E. S. Malotaux, C. De Martino, M. Spirito, D. Cavallo, A. Neto, and N. Llombart, “Wideband double leaky slot lens antennas in CMOS technology at submillimeter wavelengths,” *IEEE Transactions on Terahertz Science and Technology*, vol. 10, no. 5, pp. 540–553, 2020.

[15] L. Liu, S. M. Rahman, Z. Jiang, W. Li, and P. Fay, “Advanced terahertz sensing and imaging systems based on integrated III-V interband tunneling devices,” *Proceedings of the IEEE*, vol. 105, no. 6, pp. 1020–1034, 2017.

[16] R. A. Lewis, “A review of terahertz detectors,” *Journal of Physics D: Applied Physics*, vol. 52, no. 43, p. 433001, 2019. [Online]. Available: http://dx.doi.org/10.1088/1361-6463/ab31d5

[17] Z. Ahmad and O. K. K, “THz detection using pn-well diodes fabricated in 45-nm CMOS,” *IEEE Electron Device Letters*, vol. 37, no. 7, pp. 823–826, 2016.

[18] R. Han, Y. Zhang, D. Coquillat, H. Videlier, W. Knap, E. Brown, and O. K. K, “A 280-GHz Schottky diode detector in 130-nm digital CMOS,” *IEEE Journal of Solid-State Circuits*, vol. 46, no. 11, pp. 2602–2612, 2011.

[19] R. Han, Y. Zhang, Y. Kim, D. Y. Kim, H. Shichijo, E. Afshari, and O. K. K, “Active Terahertz imaging using Schottky diodes in CMOS: Array and 860-GHz pixel,” *IEEE Journal of Solid-State Circuits*, vol. 48, no. 10, pp. 2296–2308, 2013.

[20] D. Y. Kim, S. Park, R. Han, and O. K. K, “Design and demonstration of 820-GHz array using diode-connected NMOS transistors in 130-nm CMOS for active imaging,” *IEEE Transactions on Terahertz Science and Technology*, vol. 6, no. 2, pp. 306–317, 2016.

[21] U. R. Pfeiffer, J. Grzyb, H. Sherry, A. Cathelin, and A. Kaiser, “Toward low-NEP room-temperature THz MOSFET direct detectors in CMOS technology,” in *2013 38th International Conference on Infrared, Millimeter, and Terahertz Waves (IRMMW-THz)*, 2018, Conference Proceedings, pp. 1–2.

[22] S. Sankaran and O. K. K, “Schottky barrier diodes for millimeter wave detection in a foundry CMOS process,” *IEEE Electron Device Letters*, vol. 26, no. 7, pp. 492–494, 2005.

[23] I. Mehdi, J. V. Siles, C. Lee, and E. Schlecht, “THz diode technology: Status, prospects, and applications,” *Proceedings of the IEEE*, vol. 105, no. 6, pp. 990–1007, 2017.

[24] R. Jain, R. Zatta, J. Grzyb, D. Harame, and U. R. Pfeiffer, “A Terahertz direct detector in 22nm FD-SOI CMOS,” in *2018 13th European Microwave Integrated Circuits Conference (EuMIC)*, 2018, Conference Proceedings, pp. 25–28.

[25] E. Shaulov, S. Jameson, and E. Socher, “A zero bias J-band antenna-coupled detector in 65-nm CMOS,” *IEEE Transactions on Terahertz Science and Technology*, vol. 11, no. 1, pp. 62–69, 2021.

[26] U. R. Pfeiffer and E. Ojefors, “A 600-GHz CMOS focal-plane array for terahertz imaging applications,” in *Solid-State Circuits Conference, 2008. ESSCIRC 2008. 34th European*, 2008, Conference Proceedings, pp. 110–113.

[27] A. Lisauskas, U. Pfeiffer, E. Öjefors, P. H. Bolìvar, D. Glaab, and H. G. Roskos, “Rational design of high-responsivity detectors of terahertz radiation based on distributed self-mixing in silicon field-effect transistors,” *Journal of Applied Physics*, vol. 105, no. 11, p. 114511, 2009. [Online]. Available: https://aip.scitation.org/doi/abs/10.1063/1.3140611

[28] S. Boppel, A. Lisauskas, M. Mundt, D. Seliuta, L. Minkevicius, I. Kasalynas, G. Valusis, M. Mittendorff, S. Winnerl, V. Krozer, and H. G. Roskos, “CMOS integrated antenna-coupled field-effect transistors for the detection of radiation from 0.2 to 4.3 THz,” *IEEE Transactions on Microwave Theory and Techniques*, vol. 60, no. 12, pp. 3834–3843, 2012.

[29] M. Dyakonov and M. Shur, “Detection, mixing, and frequency multiplication of terahertz radiation by two-dimensional electronic fluid,” *IEEE. Trans. Electron Dev.*, vol. 43, no. 3, pp. 380–387, 1996.

[30] M. A. Andersson and J. Stake, “An accurate empirical model based on Volterra series for FET power detectors,” *IEEE Trans. on Microw. Theory and Techn.*, vol. 64, no. 5, pp. 1431–1441, 2016.

[31] M. I. W. Khan, S. Kim, D. Park, H. Kim, S. Han, and S. Lee, “Nonlinear analysis of nonresonant THz response of MOSFET and implementation of a high-responsivity cross-coupled THz detector,” *IEEE Transactions on Terahertz Science and Technology*, vol. 8, no. 1, pp. 108–120, 2018.

[32] A. M. Cowley and H. O. Sorensen, “Quantitative comparison of solid-state microwave detectors,” *IEEE Transactions on Microwave Theory and Techniques*, vol. 14, no. 12, pp. 588–602, 1966.

[33] G. Rieke, *Detection of Light: from the Ultraviolet to the Submillimeter*. Cambridge University Press, 2003.

[34] A. Luukanen, R. Appleby, M. Kemp, and N. Salmon, *Millimeter-wave and terahertz imaging in security applications*. Springer, 2012, pp. 491–520.

[35] C. Dietlein, A. Luukanen, F. Meyer, Z. Popovic, and E. Grossman, “Phenomenology of passive broadband terahertz images,” in *4th ESA Workshop on Millimetre-wave Technology and Applications*, 2006, Conference Proceedings, pp. 405–410.

[36] L. Galatro, A. Pawlak, M. Schroter, and M. Spirito, “Capacitively loaded inverted CPWs for distributed TRL-based de-embedding at (sub) mm-waves,” *IEEE Transactions on Microwave Theory and Techniques*, vol. 65, no. 12, pp. 4914–4924, 2017.

[37] K. S. Champlin and G. Eisenstein, “Cutoff frequency of submillimeter Schottky-barrier diodes,” *IEEE Transactions on Microwave Theory and Techniques*, vol. 26, no. 1, pp. 31–34, 1978.

[38] R. A. Hadi, H. Sherry, J. Grzyb, Y. Zhao, W. Forster, H. M. Keller, A. Cathelin, A. Kaiser, and U. R. Pfeiffer, “A 1 k-pixel video camera for 0.7-1.1 Terahertz imaging applications in 65-nm CMOS,” *IEEE Journal of Solid-State Circuits*, vol. 47, no. 12, pp. 2999–3012, 2012.

[39] R. A. Hadi, J. Grzyb, B. Heinemann, and U. R. Pfeiffer, “A Terahertz detector array in a SiGe HBT technology,” *IEEE Journal of Solid-State Circuits*, vol. 48, no. 9, pp. 2002–2010, 2013.

[40] S. J. Orfanidis, “Electromagnetic waves and antennas,” 2002.

[41] J. Grzyb, H. Sherry, Y. Zhao, R. Al Hadi, A. Cathelin, A. Kaiser, and U. Pfeiffer, “Real-time video rate imaging with a 1k-pixel THz CMOS focal plane array,” vol. 8362, Conference Proceedings, pp. 83 620C–83 620C–12. [Online]. Available: http://dx.doi.org/10.1117/12.919218

[42] G. Carluccio and M. Albani, “Efficient adaptive numerical integration algorithms for the evaluation of surface radiation integrals in the high-frequency regime,” *Radio Science*, vol. 46, no. 5, 2011. [Online]. Available: https://agupubs.onlinelibrary.wiley.com/doi/abs/10.1029/2010RS004623